Article

Design and Experiment on Heat Dissipation Structures of Ducted Fan Motor for Flying Electric Vehicle

Ye Li [1,2], Qi Li [1,2,3,*], Tao Fan [1,2,3], Xuhui Wen [1,2,3] and Junhui Xiong [4]

1   Institute of Electrical Engineering, Chinese Academy of Sciences, Haidian District, Beijing 100190, China; liye@mail.iee.ac.cn (Y.L.); fantao@mail.iee.ac.cn (T.F.); wxh@mail.iee.ac.cn (X.W.)

2   Key Laboratory of High Density Electromagnetic Power and Systems (Chinese Academy of Sciences), Institute of Electrical Engineering, Chinese Academy of Sciences, Haidian District, Beijing 100190, China

3   University of Chinese Academy of Sciences, Shijingshan District, Beijing 100049, China

4   Ningbo Institute of Materials Technology & Engineering, Chinese Academy of Sciences, Ningbo 315201, China; xiongjunhui@nimte.ac.cn

*   Correspondence: hustliqi@mail.iee.ac.cn; Tel.: +86-10-82547013

Abstract: Ducted fan motors play a crucial role in promoting various applications of flying electric vehicles. In ducted fan motor systems, motor performance affects the speed of the fan, the flow field of the fan affects the thermal field of the motor, and the thermal field influences the performance of the motor. The coupling model between fan static thrust, motor power, and motor temperature rise is established in this paper. After confirming the external dimensions of the motor, three cooling schemes of the motor casing are designed. The casing forms are as follows: model 1 with smooth surface, model 2 with circular fins, and model 3 with longitudinal fins. The optimization work was carried out on the geometric dimensions of two types of fins for model 2 and model 3, and the static thrust and heat transfer performance of the motors were calculated. This study proposes that the ratio of thrust-to-temperature rise is an indicator for future optimization design of ducted fan motors. Model 3 with longitudinal fins has a higher thrust-to-temperature rise ratio. The thrust temperature rise in model 3 has increased by 24.77% compared to model 1.

Keywords: flying electric vehicle; ducted fan; thermal management

1. Introduction

Ducted fan motors play a crucial role in promoting various applications of flying electric vehicles. Their unique characteristics, including vertical takeoff and landing (VTOL) capability, short takeoff and landing (STOL) and slow-flight capability, noise reduction, and improved energy efficiency, make them highly promising in the realm of flying vehicles [1–6]. The future development of ducted fan motors will focus on achieving higher power density, higher cruising speed, longer battery life, and higher task load capacity.

In the design of a ducted fan motor, the rotary blades serve as the energy source by accelerating airflow through the duct, while the duct plays a crucial role in focusing and diffusing the airflow. The heat dissipation form of a motor is generally forced convection, which leads to rapid heating inside the motor and controller components under high-power conditions. Additionally, the enclosed installation within the compact wheel hub exacerbates the thermal issues.

In the thermal design of ducted fan motors, various challenges exist: (1) Ducted fan motors are typically installed within small-sized ducts, which have limited installation space. (2) Due to system limitations, air cooling is commonly employed, resulting in low cooling efficiency. (3) The structure of heat dissipation should not impact the internal flow field of the ducted fan in order to maintain the fan's performance efficiency. As a result, the ducted fan motor system involves interconnected issues related to the electromagnetic, thermal, and flow fields of the fan [7].

Many researchers have paid attention to ducted fan motors. For example, in the aerodynamic aspect of ducted fans, Deng conducted experimental evaluations on the aerodynamic performance of ducted fans by measuring force, pressure, and PIV. To comprehensively understand the aerodynamic characteristics of the ducted fan, Deng studied variations in rotational speed, inlet angle, forward flight speed, and ground clearance. Wind tunnel tests were also conducted [8]. Guo proposed an efficient design method for ducted propeller blades based on blade element momentum theory [9]. Specifically, the inflow angle and angle of attack were corrected through CFD calculations. The correction coefficients were obtained by inversely solving the CFD results. After preliminary design, by iteratively solving the correction coefficients and redesigning, a ducted propeller that meets the design requirements can be quickly obtained. The design of ducted propellers under different conditions showed that this design approach typically requires only two rounds of CFD calculations and redesign to meet the design specifications efficiently while maintaining good design accuracy. Numerical simulation was used to validate the aerodynamic performance of a NASA nacelle fan test model [10]. The impact of the blade tip clearance and the axial relative position between the rotor disk and the duct on the flow field, as well as the aerodynamic performance of the ducted fan in hover, was revealed. The findings indicated that a larger propeller tip clearance weakens the suppression of propeller tip vortices, leading to a significant reduction in the aerodynamic performance of the ducted fans. As the rotor disk approaches the baseline position at the duct outlet, the velocity within the duct changes, leading to a decrease in thrust. Sun presented the method that couples the panel with the wake model of the propeller slipstream tube [11]. Utilizing this method, a quick optimization design of the ducted fan casing exterior was conducted. Fluid flow analysis based on CFD shows that the optimized expansion angle of the duct wall was decreased, and the inflow velocity at the propeller inlet was decreased, thereby increasing its efficiency. As a result, the overall propulsion efficiency of the ducted fan improved by 20.7%. Refs. [12–14] also conducted research on geometric variables and tension calculations related to axial fans.

The study of the motor in the ducted fan motor system can benefit from existing motor research findings. Effective thermal management is crucial for ensuring optimal performance and reliability of the motor. The cooling system's heat transfer and cooling efficiency hinge on a variety of factors, including the coolant flow location, cooling surface design, coolant supply parameters, and the thermal properties of the coolant [15,16]. The specific power and temperature rise in the motor under fixed outer diameter constraints were analyzed in the article [17]. Additionally, the influence of the split ratio on current load and loss was examined to optimize motor performance. Two air-cooled cooling modes were designed, and the reliability and effectiveness of the motor were verified through simulation. Hu designed an air cooling system for the motor in the electric ducted fan propulsion system [18]. It featured a cooling guide vane with a heat pipe (CGVHP). The heating end of the heat pipe was inserted into the stator end winding, while the cooling end was located inside the cooling guide vane. By using the heat pipe, the heat generated in the winding was effectively transferred to the cooling guide vane. The simulation results demonstrate that under peak power conditions of 15.7 kW, the proposed CGVHP system can decrease the winding temperature of the motor by over 25.5 °C. Huang proposed a dual-motor drive architecture for a counter-rotating ducted fan [19]. An annular heat conduction sheet structure for adjusting the thermal coupling degree between the two motors has also been proposed. This method effectively improves the heat dissipation performance of the motor and optimizes the temperature rise distribution between the front and rear motors. Yu designed an enhanced air-cooling heat dissipation system [20]. Four distinct air-cooled heat sink configurations with fin heights of 3 mm, 6 mm, 9 mm, and 12 mm have been developed. A comparative evaluation of the cooling efficiency at different air velocities has been performed through engineering approximations and computational fluid dynamics (CFD) simulations. Additionally, an experimental setup has been established to conduct ground tests to confirm and validate the obtained results.

Chen solved the issue of overheating in a ducted fan motor during operation [21]. An electromagnetic finite element model of the motor was first established using the Maxwell 2D software to calculate losses. The losses were coupled as heat sources into the ANSYS Workbench 2021R1 software for a magnetic–thermal coupling analysis. To alleviate the temperature rise in the motor, the proposition of attaching heat sinks to the motor casing was made, with an analysis conducted on three different shapes of heat sinks—rectangular, trapezoidal arc, and triangular. Jin introduces a motor design model based on the fan hub-to-tip ratio, which demonstrates the significant potential of the thermal coupling effect between fan aerodynamic design and motor cooling design in enhancing motor power density in electric propulsion systems [22]. A smaller hub-to-tip ratio is preferred, ensuring power and cooling balance.

In ducted fan motor systems, motor performance affects the speed of the fan, the flow field of the fan affects the thermal field of the motor, and the thermal field of the motor combined with the magnetic field of the motor influences the performance of the motor, resulting in a coupled issue. Currently, research tends to focus on isolated studies of fans and motors. This study focuses on an interior permanent magnet synchronous motor system. The primary aim of this article is to enhance the heat dissipation of a ducted fan motor while considering the airflow within the duct. This study initially examines the relationship between fan static thrust, motor power, and motor temperature rise. Three cooling surface designs are devised for a specific fan motor, and the static thrust and heat transfer performance of these motors are calculated. Three types of motors are processed and subjected to thermal testing. Simultaneously, the Taguchi experimental method was used to optimize two heat dissipation enhancement designs. The research proposes the ratio of thrust to the temperature rise as an indicator for future optimization designs of ducted fan motors and presents a comparison of this ratio for the three designs.

2. Collaborative Design of Fan and Motor

The ducted fan is an electrically driven propeller enclosed within a duct. The propeller is a device that converts the power of the motor into a pulling force. According to the momentum theory, a propeller is considered to be a disc with an infinite number of advancing blades, with a uniform distribution of tension generated on the disc. If the disk is assumed to be infinitely thin, a pressure difference exists before and after the disk, while the axial velocity remains equal on both sides. To facilitate the solution process, it is assumed that the gas is an ideal compressible fluid. By applying the Bernoulli equation, the thrust of the propeller can be determined. Also, in accordance with the momentum theorem, the force exerted by the propeller on the airflow (which is equal to the propeller's thrust but in the opposite direction) should be equivalent to the incremental momentum of the propeller disk.

$$T_c = \frac{\pi}{4}\left(D_{tip}^2 - D_{m,out}^2\right)v_{out}\rho_{air}v_{out}, \tag{1}$$

where T_c is the static thrust of ducted fan (N), D_{tip} is the outer diameter of the propeller hub (mm), $D_{m,out}$ is the outer diameter of the motor (mm), v_{out} is the outlet flow velocity of duct (m/s), ρ_{air} is air density (kg/m^3).

$$P_c = \frac{1}{2}m\left(v_{out}^2 - v_{in}^2\right), \tag{2}$$

where P_c is the theoretical minimum aerodynamic power (W), v_{in} is the inlet flow velocity of the duct (m/s). The calculation of static thrust for an axial flow fan is based on an idealized model. This calculation can be influenced by factors like air density, fan efficiency, and motor efficiency in practical situations. Thus, this formula provides a fundamental calculation method.

$$P_{propeller} = P_{motor} = 2\pi nT/60, \tag{3}$$

where $P_{propeller}$ and P_{motor} represent the power of the rotor blades and the propulsion motor (W), respectively, with T and n denoting torque (N·m) and the rotational speed (rpm).

$$P_{m,out} = \omega_m T_m \propto n B_g A_I D_{m,inner}^2 L_e k_w, \tag{4}$$

$$A_I = \frac{Q n_s I_s}{\pi D_{m,inner}}, \tag{5}$$

where $P_{m,out}$ is the motor output power (W), ω_m is motor speed (rad/s), T_m is motor torque (N·m), B_g is based on the amplitude of the fundamental wave of air gap magnetic density (T), A_I is line load (A/m), L_e is effective axial length of iron core (m), K_w is winding factor, Q is number of slots, n_s is number of conductors per slot, and I_s is the current (Arms).

$$Q_{out} = h A_{motor}(T_{wall} - T_{air}), \tag{6}$$

$$P_{loss,cu} \propto A_I J, \tag{7}$$

$$J = \frac{I_s}{S_n} = \frac{Q n_s I_s}{\frac{\pi}{4}\left(D_{m,out}^2 - D_{m,in}^2\right) k_{slot}}, \tag{8}$$

where Q_{out} is heat dissipating capacity (W), h is convectional heat transfer coefficient (W/(m²·K)), A_{motor} is the external surface area of the motor (m²), and T_{wall} is the average temperature of the outer surface wall of the motor (K), T_{air} is the temperature of air (K). $P_{loss,cu}$ is the copper loss (W), k_{slot} is the spacer factor.

The coupling model between fan static thrust, motor power, and motor temperature rise was established through the analysis above. When analyzing the relationship between the outer diameter of the motor and the outer diameter of the propeller hub (denoted as k_d), it becomes evident that a k_d value of approximately 0.73 and a ratio of the inner diameter to the outer diameter of the motor (k_{out}) at 0.25, result in a minimal temperature rise in the motor. As k_{out} increases, the power output also increases directly. The optimal range for k_d falls between 0.72 and 0.74, while k_{out} ranges from 0.25 to 0.4. Within this parameter range, the temperature rise in the motor is relatively low, while there is a clear trend of increased power output as the k_{out} value rises. When the k_d value is around 0.72, fixing the D_{tip} (outer diameter of propeller hub) to 390 mm is recommended. At a k_{out} value less than 0.33, the temperature rise in the motor tends to decrease as k_{out} increases. For k_{out} values below 0.33, the temperature rise in the motor decreases as k_{out} increases. On the contrary, when the value of k_{out} exceeds 0.33, the motor temperature rises with an increase in k_{out}. It is important to note that as k_{out} increases, the power output of the motor also increases. The optimal k_{out} value, at which both power output and temperature rise criteria are met, is approximately 0.26.

Therefore, we are optimizing a duct fan motor with a D_{tip} of 390 mm, $D_{m,out}$ (outer diameter of motor) is 100 mm, and k_d is 0.7. After completing the benchmark size design, this article explores the heat dissipation performance of the motor under three types of motor casing forms. Table 1 shows the fin forms and main geometric dimensions of fins, including their height, width, and quantity. The casing forms are as follows: model 1 has a smooth surface, with no fins installed on the surface; model 2 has circular fins, and the fin height is 1 mm, the fin width is 8mm, and the number of fins is 8; model 3 has longitudinal fins. In model 3, the front half of the motor length has 30 fins, while the back half has 60 fins. Three types of motor forms are provided in Figure 1.

The thermal design of the motor involves evaluating the coupling effect between the ducted fan and the motor, followed by assessing the impact of the thermal design on the thrust of the fan. Subsequently, external convection environment considerations are calculated before performing the thermal calculation of the motor body.

Table 1. Model parameters.

	Model 1	Model 2	Model 3
Fin form	nothing	circular fins	longitudinal fins
Fin height/mm	0	1	4
Fin width/mm	0	8	1/
Number of fins	0	15	30/60

| (a) | (b) | (c) |
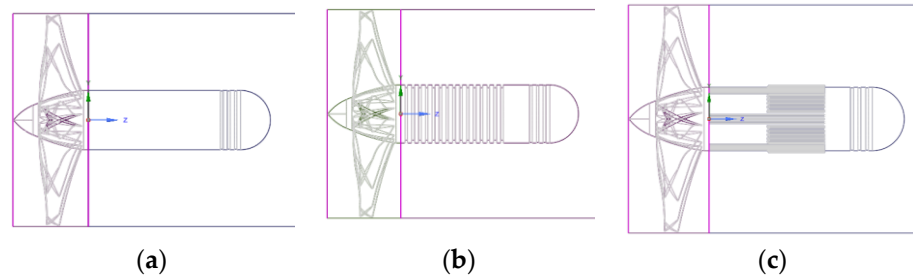
Figure 1. The different cooling structures of motors: (**a**) the motor casing of model 1; (**b**) the motor casing of model 2; (**c**) the motor casing of model 3.

3. Flow Field Simulation

This part focuses on how the external shape of a motor system affects the aerodynamic performance of a ducted fan. The aerodynamic characteristics of ducted fans are complex, primarily due to the interaction between the duct and the fan. Parameters that affect the efficiency of ducted fans include duct height, rotor mounting position, clearance between rotor and duct wall, number of blades, speed, and other factors. Various computational models for axial fans exist, such as the slip flow theory, blade element theory, and vortex model. However, this study specifically examines how the cooling design of the motor's surface disrupts airflow, leading to changes in the duct thrust. To evaluate the impact of heat dissipation design, numerical simulation was employed, focusing solely on axial thrust calculations of the models without analyzing fan parameters.

The numerical simulation of the flow field of the ducted fan motor system was performed using the ANSYS 2021R1 software. The simulation employs the finite volume method and Multiple Reference Frames (MRF) approach to model the flow field within the duct. In the MRF technique, a closed, approximately cylindrical zone called the rotating domain is created around the propeller to replicate its rotational motion. The stationary domain of the system consists of the remaining components, with an interface connecting the rotating and stationary domains for flux exchange. This interface only needs surface overlap, making mesh generation easier.

The simulation model shown in Figure 2a includes an inlet, outlet, duct, rotating fan blade, motor, and controller. The fan blade region is set as the rotating domain with a speed of 10,000 rpm, and the blades and the outer walls of the motor are set as non-slip walls. The motor rotates the blades to simulate the initial takeoff operation of the ducted fan. The boundary condition of the outlet is set as outflow; the fluid is an ideal compressible gas. Mesh division is performed using ANSYS Fluentmeshing 2021R1 software, with fine grid refinements at the wall surfaces, as shown in Figure 2b.

The computed results are illustrated in Figure 3. Comparing the airflow passing through the outer wall of the motor, the flow fields of model 1 and model 2 appear more symmetrical. There is a velocity loss at the fins of model 3, while the velocity loss at the smooth walls between the fins is noticeably reduced. The maximum velocity near the outer wall of the motor is observed with model 1.
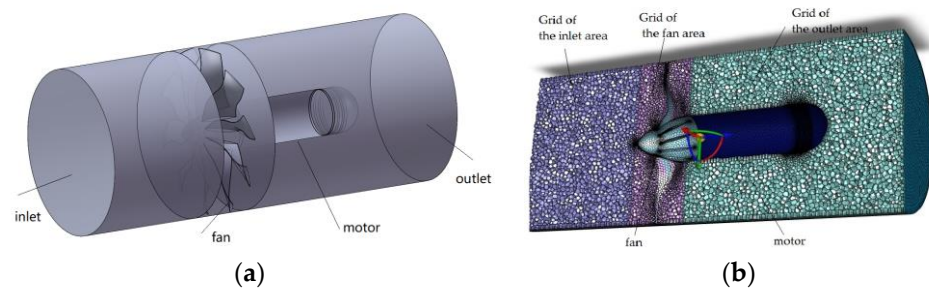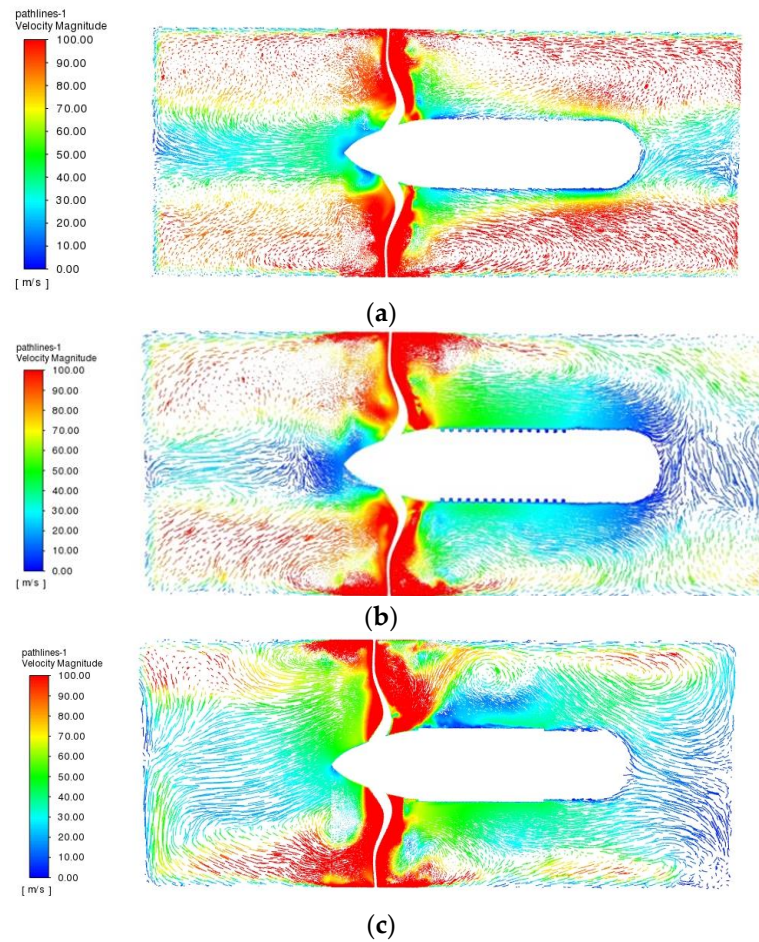
Figure 2. Simulation model: (**a**) geometric model; (**b**) grids.

Figure 3. The velocity of the outer surface motor diagram: (**a**) the velocity of model 1; (**b**) the velocity of model 2; (**c**) the velocity of model 3.

The presence of fins has a certain impact on the overall performance of the ducted fan. The axial thrusts are calculated as follows: axial thrusts of models 1–3 are represented as 553.37 N, 513.28, and 492.87 N, consecutively.

The results are shown in Figure 4. From the results, it was found that compared to a smooth surface of casing, adding fins to the casing reduces the thrust of the ducted fan. Longitudinal fins have more impact on thrust compared to circular fins. The thrust of model 3 decreased by 16.3% compared to that of model 1. The thrust of model 2 decreased by 7.2% compared to that of model 1.
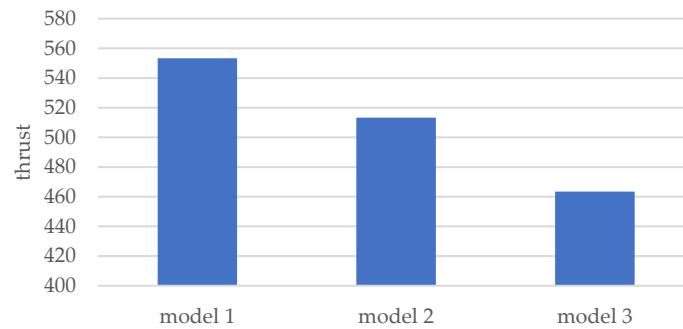
Figure 4. The thrust of the ducted fan motors.

4. Thermal Calculation

Furthermore, we assessed the thermal performance of three types of motor casings. The stator of an electric motor, which is the primary heat source, directly contacts the housing. The internal fluid in the duct flows externally over the surface of the housing for convective heat transfer. This study focuses on comparing and analyzing the steady-state operating conditions of the ducted fan motor.

4.1. Numerical Calculation

The key challenge in solving the heat dissipation problem is determining the convective heat transfer coefficient under air cooling conditions. The first step is to calculate the convective heat transfer coefficient on the outer surface of the motor. The calculation model and grids are shown in Figure 5. The simplified model assumes that heat only dissipates from the motor housing, the heat flux on the outer surface of the motor housing is uniformly distributed, and external air flows axially and circumferentially, neglecting gravity. The boundary conditions are set as follows: an inlet flow velocity of 8 m/s (provided by the experimental setup) and the heat source is 470 W.
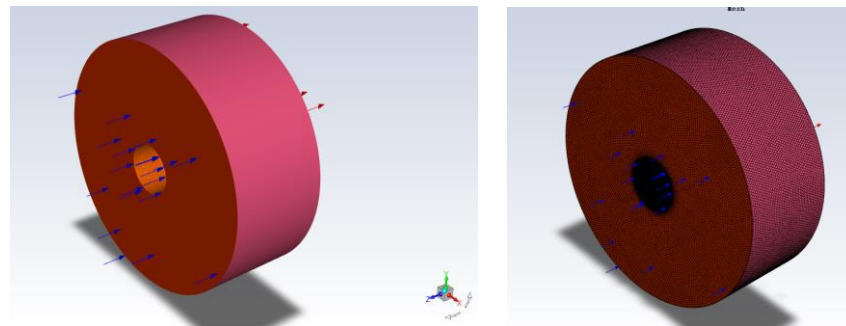

Figure 5. The model and grids for convective heat transfer coefficients.(The blue arrows represent the inlet direction, and the red arrows represent the outlet direction).

Equation (9) represents the formula for calculating the average convective heat transfer coefficient, where h is the average convective heat transfer coefficient (W/(m^2·K)), Q is the amount of heat generated by the motor (W), A is the heat transfer surface area (m^2), $T_{wall,ave}$ is the average temperature of the heat transfer surface (K), and T_{air} is the temperature of the fluid (K).

$$h = \frac{Q}{A(T_{wall,ave} - T_{air})}, \tag{9}$$

According to Equation (9), Q, T_{air}, and A are known quantities. $T_{wall,ave}$ can be obtained through simulation calculations, and the convection heat transfer coefficient on the surface of the motor casing can be calculated. The same method can be applied to calculate the convective heat transfer coefficient of the casing surfaces for models 2 and 3.

Next, the internal temperature field of the motor stator is calculated. To optimize computational resources, a full model of a single stator unit within the motor is developed, encompassing the housing, iron core, windings, impregnating varnish, and insulation paper for comparative thermal evaluation inside the motor, as shown in Figure 6.
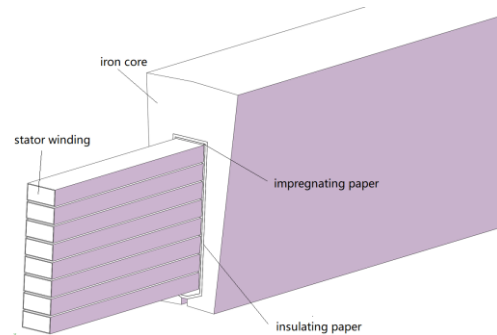

Figure 6. The model of the stator.

The motor model is simplified as follows: (1) the fact that the iron core is superposed by a single punching sheet and regards the iron core as a whole is ignored; (2) the heat transfer mode in the form of thermal radiation is ignored; (3) the heat source is uniformly distributed in both the iron core and the winding. (4) the convection heat transfer coefficient of the motor casing is simulated in the preceding text, and the thermal simulation of the motor is carried out using the third type of boundary conditions. Therefore, the simplified model is established. The materials of the simulation model are shown in Table 2.

Table 2. Material properties.

Materials	Density (kg/m³)	Specific Heat Capacity J/(kg·K)	Thermal Conductivity/(m·K)
Motor casing	2710	902	110
Iron core	7849	481	45/45/19
Stator winding	8930	386	398
Insulating paper	1250	1660	0.144
Impregnating varnish	1390	1172	0.155

Under long-term working conditions, the iron loss of the motor is 166 W, and the copper loss is 172 W (data sourced from experimental values). The calculated results in Figure 7 show that the maximum temperatures of the three motors are 424 K, 401 K, and 386 K, respectively. The temperature rise decreases by 18.5% for windings with circular fins compared to windings with a smooth surface and by 30.6% for windings with longitudinal fins. It is evident that optimizing the heat dissipation on the outer surface of the motor is significantly effective in increasing the power density of the motor.
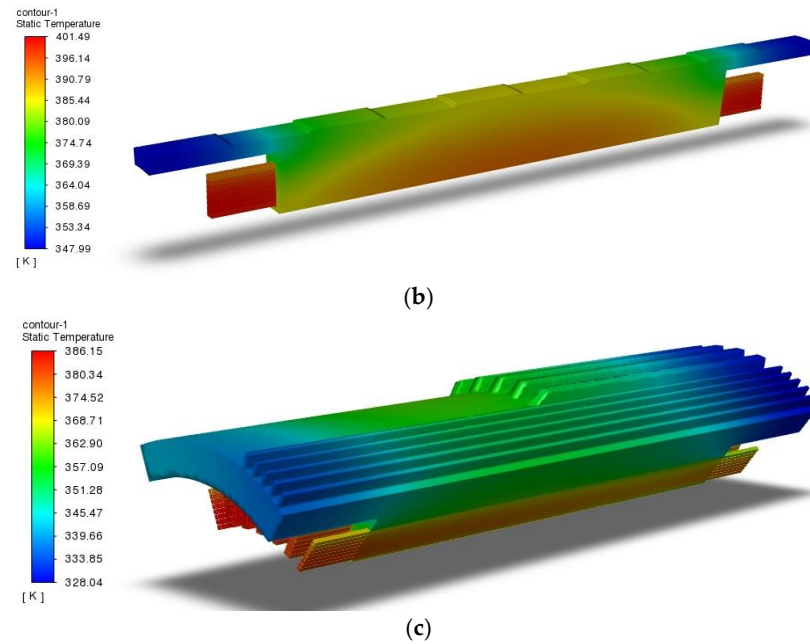

(**a**)

Figure 7. *Cont.*

(**b**)

(**c**)
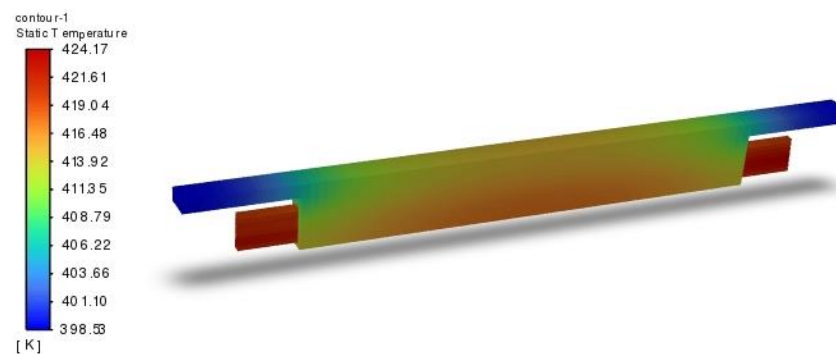
Figure 7. The simulation results of motors: (**a**) the temperature of model 1; (**b**) the temperature of model 2; (**c**) the temperature of model 3.

4.2. Experimental Verification

Three motors with different heat dissipation designs were built and tested to verify the design's effectiveness. The motor core component and experimental platform can be observed in Figure 8a,b. The experimental platform comprises the tested motor, controller, cooling system, temperature data collector, and other essential components. The temperature data acquisition system model GL820 is shown in Figure 8c. The thermal resistance for temperature measurement is buried at the end of the winding. The thermal resistance is Pt1000, shown in Figure 8d. The three prototypes designed are shown in Figure 9. To facilitate the airflow testing, a fan was used in place of the ducted fan, and the airspeed was measured using an anemometer. This experiment serves to test the performance of different methods and validate the accuracy of the simulation methods discussed earlier.

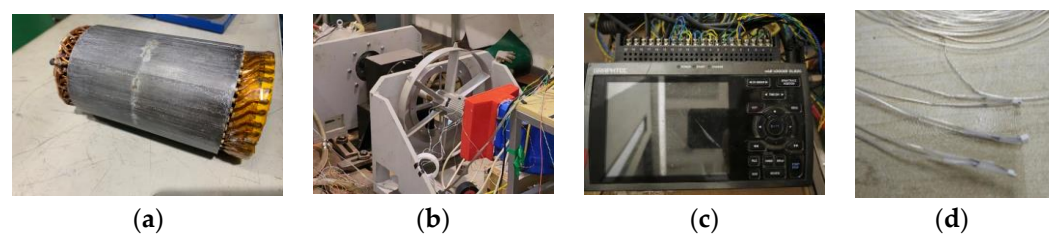(**a**)　　　　　(**b**)　　　　　(**c**)　　　　　(**d**)

Figure 8. The motor core component and test platform: (**a**) motor core component; (**b**) test platform; (**c**) temperature digital acquisition system; (**d**) thermal resistance of Pt1000.

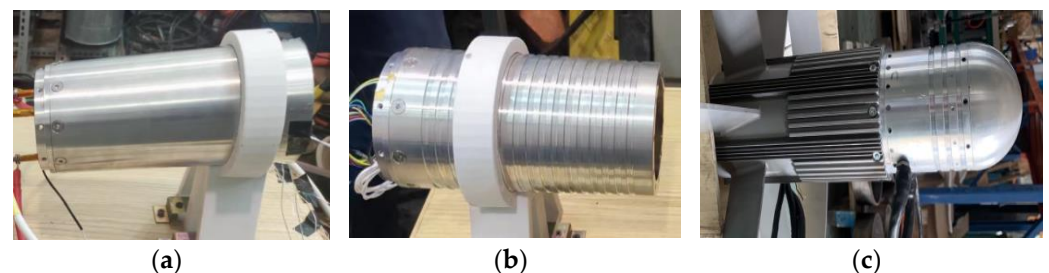(**a**)　　　　　(**b**)　　　　　(**c**)

Figure 9. Prototypes: (**a**) the prototype of model 1; (**b**) the prototype of model 2; (**c**) the prototype of model 3.

The main equipment used during the experiment is shown in Table 3.

Table 3. Testing equipment.

Equipment	Specifications	Manufacturer	City	Country
DC power supply	VEADL-120-1000	VARIED	Suzhou	China
Torque speed sensor	T40B	HBM	Darmstadt	Germany
Oscilloscope	DS1104	YOKOGAWA	Tokyo	Japan
Power analyzer	LMG671	ZES ZIMMER	Frankfurt	Germany
Temperature acquisition system	GL820	GRAPHTEC	Yokohama	Japan
Micro resistance tester	RM3548	HIOKI	Shanghai	China
current probe	A621-1000	Tektronix	Shanghai	China

In this experiment, copper loss and iron loss are critical data points. Indirect measurement methods are utilized to determine values such as resistance, current, voltage, torque, and speed, as direct measurement of these parameters is not feasible. The credibility of experimental results is critically influenced by the uncertainty associated with these indirect measurements. Therefore, an analysis of the uncertainty of these measurements is essential for ensuring the validity and reliability of the experimental findings.

The quadratic power method is used to estimate the parameters and their functions that follow a normal distribution. The specific description is: assuming $R = R(X_1, X_2, \ldots, X_N)$, the N independent variables $X_1, X_2, \ldots, X_N$ each follow a normal distribution for their uncertainties. ΔR (the uncertainty of R) and $\Delta R/R$ (the relative uncertainty of R) are determined by Equations (10) and (11).

$$\Delta R = \sqrt{\sum_{i-1}^{N}\left(\frac{\partial R}{\partial X_i}\Delta X_i\right)^2}, \tag{10}$$

$$\frac{\Delta R}{R} = \sqrt{\sum_{i-1}^{N}\left(\frac{\Delta X_i}{X_i}\right)^2}, \tag{11}$$

$$\left(\frac{\Delta P_{cu}}{P_{cu}}\right) = \sqrt{\left(\frac{\Delta I}{I}\right)^2 + \left(\frac{\Delta R_{cu}}{R_{cu}}\right)^2} = \sqrt{(0.02\%)^2 + (0.02\%)^2} = 0.028\%, \tag{12}$$

$$\begin{aligned}\left(\frac{\Delta P_{fe}}{P_{fe}}\right) &= \sqrt{\left(\frac{\Delta P}{P}\right)^2 + \left(\frac{\Delta n}{n}\right)^2 + \left(\frac{\Delta T}{T}\right)^2 + \left(\frac{\Delta P_{cu}}{P_{cu}}\right)^2}\\ &= \sqrt{(0.025\%)^2 + (0.01\%)^2 + (0.01\%)^2 + (0.028\%)^2} = 0.039\%\end{aligned} \tag{13}$$

The given current has an effective value of 21Arms, and the motor speed is 3000 rpm. The iron loss of the motor is 166 W, and the copper loss is 172 W (the data come from measured values). Table 4 displays the experimental and simulation results of the winding temperature. Through experiments, it was found that the accuracy of the above calculation method is relatively high and can be used for extended research on later operating conditions.

Table 4. Experimental results.

	Model 1	Model 2	Model 3
Experimental data/K	431	417	394
Simulation data/K	424	401	386

4.3. Optimization Design of Taguchi Experiment

To enhance heat dissipation, both model 2 and model 3 add fins on the surface of the motor. The optimization of geometric parameters is aimed at maximizing heat dissipation

efficiency for two specific types of fins: circular fins and longitudinal fins. The design is optimized to determine the motor casing form that offers improved heat dissipation performance.

The Taguchi experiments based on the range analysis model are a highly effective approach for investigating multiple factors at various levels [23–25]. This optimization testing method comprises the following steps: (1) the experimental purposes are cleared, and the experimental index is determined; (2) the experimental factors and their corresponding levels are determined (factors changes); (3) the experimental data are subjected to range analysis to assess the impact of different factors on the testing indicators.

The purpose of the experiment is to reduce the temperature rise in the motor by designing the motor casing. Key design parameters (experimental factors) that are optimized include fin height (H_f), fin width (W_{th}), and the ratio of slot width to fin width (R_{hw}). In this work, H_f may vary between 1 mm and 5 mm, W_{th} ranges between 1 mm and 5 mm, and R_{hw} ranges between 1 and 3.

This article studies three factors and five levels (the values of each factor are a level). Refer to Table 5 for the Taguchi experiment table, which includes three factors and five levels for optimization experiments. The maximum temperature of the motor winding under consistent heat dissipation conditions and the heat source is calculated using MotorCAD 14.1.5 software. The optimization process is carried out using the Taguchi experimental method. The motor temperature rise is calculated for two different fin forms across 25 sets of geometric parameters. Two types of fin forms are shown in Figure 10. The highest temperature values of winding for each test point in the numerical calculation are shown in Tables 6 and 7.

Table 5. Taguchi experiment design.

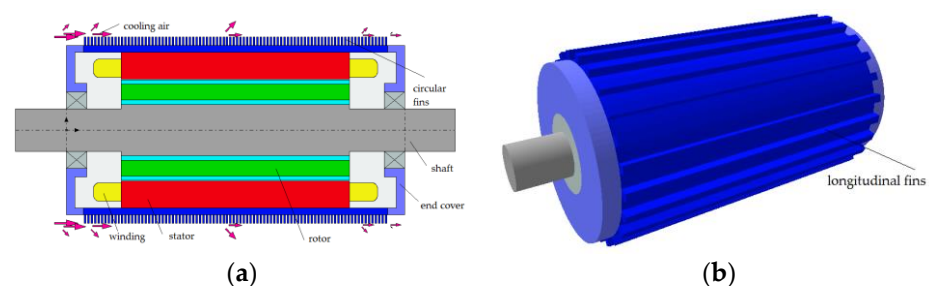| No	H_f/mm	W_{th}/mm	R_{hw}	No	H_f/mm	W_{th}/mm	R_{hw}
1	1	1	1	14	3	7	1
2	1	3	1.5	15	3	9	1.5
3	1	5	2	16	4	1	2.5
4	1	7	2.5	17	4	3	3
5	1	9	3	18	4	5	1
6	2	1	1.5	19	4	7	1.5
7	2	3	2	20	4	9	2
8	2	5	2	21	5	1	3
9	2	7	3	22	5	3	1
10	2	9	1	23	5	5	1.5
11	3	1	2	24	5	7	2
12	3	3	2.5	25	5	9	2.5
13	3	5	3				

(**a**)   (**b**)

Figure 10. Two types of fin forms: (**a**) the motor surface of circular fins; (**b**) the motor surface of longitudinal fins.

Table 6. Numerical calculation of the highest temperature of the motor winding (circular fins).

No	T_{cu}/K	No	T_{cu}/K	No	T_{cu}/K	No	T_{cu}/K	No	T_{cu}/K
1	394.0	6	380.9	11	374.3	17	370.1	21	367.9
2	419.5	7	411.8	12	407.1	17	403.6	22	378.5
3	426.9	8	419.9	13	418.9	18	398.4	23	397.4
4	430.5	9	427.1	17	411.7	19	411.3	24	409.3
5	433.8	10	421.8	18	419.8	20	418.0	25	417.6

Table 7. Numerical calculation of the highest temperature of the motor winding (longitudinal fins).

No	T_{cu}/K	No	T_{cu}/K	No	T_{cu}/K	No	T_{cu}/K	No	T_{cu}/K
1	379.4	6	350.5	11	340.7	17	336.3	21	333.7
2	385.1	7	360.6	12	351.5	17	347.2	22	340.5
3	385.3	8	364.5	13	356.7	18	351.6	23	347.1
4	384.8	9	365.9	17	359.9	19	354.4	24	351.1
5	387.5	10	371.7	18	366.0	20	356.8	25	353.9

Data processing: first, the average winding temperature for each of the three factors at five levels is calculated as shown in the table for k_1–k_5. Then, the range analysis of the experimental data of different levels belonging to the different factors is performed. We obtained the value of R_j in Equation (14). B-p is the value of the level corresponding to the minimum value of k in each factor.

$$R_j = \max\{\mathrm{I}_j/k_j, \mathrm{II}_j/k_j, \ldots\} - \min\{\mathrm{I}_j/k_j, \mathrm{II}_j/k_j, \ldots\} \tag{14}$$

The calculation results of the two types of fins are shown in Tables 8 and 9. The parameter subscripts denote different types of fins: cf for circular fins and lf for longitudinal fins. Through range analysis, the following conclusion can be seen: within the experimental range, the circular fins motor has the lowest winding temperature and the optimal structure at $H_{\text{f-cf}}$ of 5 mm, $W_{\text{th-cf}}$ of 1 mm, and $R_{\text{hw-cf}}$ of 1; the longitudinal fins motor has the lowest winding temperature and the optimal structure at $H_{\text{f-cf}}$ of 5 mm, $W_{\text{th-cf}}$ of 1 mm, and $R_{\text{hw-cf}}$ of 4 or 5.

Table 8. Range analysis of the maximum temperature of winding (surface with circular fins).

	$H_{\text{f-cf}}$/mm	$W_{\text{th-cf}}$/mm	$R_{\text{hw-cf}}$
k1	420.89	377.39	400.83
k2	412.25	404.05	405.73
k3	406.31	412.25	408.01
k4	400.23	417.93	408.99
k5	394.09	422.15	410.21
R_j	26.8	44.76	9.38
B-P	5	1	1

Table 9. Range analysis of the maximum temperature of winding (surface with longitudinal fins).

	$H_{\text{f-lf}}$/mm	$W_{\text{th-lf}}$/mm	$R_{\text{hw-lf}}$
k1	384.37	348.07	360.57
k2	362.59	356.93	360.57
k3	354.91	360.99	358.85
k4	349.21	363.17	358.15
k5	345.21	367.13	358.15
R_j	39.16	19.06	2.42
B-P	5	1	4/5

The various factors affecting the winding temperature caused by the circular fins are shown in Figure 11. The impact of $W_{\text{th-cf}}$, $H_{\text{f-cf}}$, and $R_{\text{hw-cf}}$ on winding temperature is reduced in sequence. As the $H_{\text{f-cf}}$ increases, the temperature of the motor winding gradually decreases. Lower winding temperatures are preferable. Conversely, as the $W_{\text{th-cf}}$ and $R_{\text{hw-cf}}$ increase, the temperature rise in the motor winding also increases gradually. It can be seen that among these three factors, increasing $W_{\text{th-cf}}$ has the most significant effect.
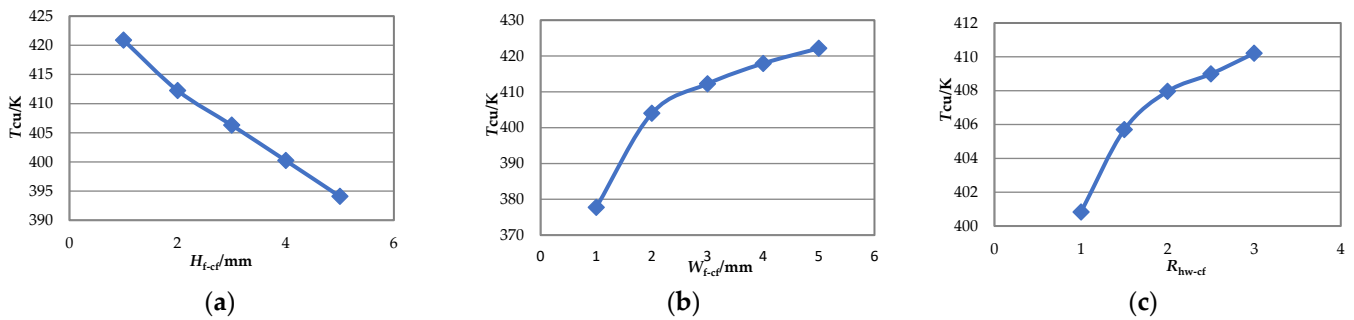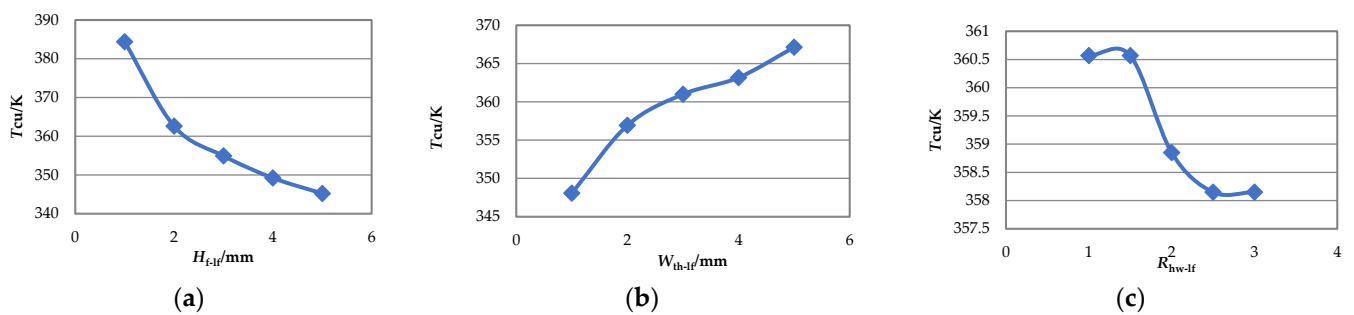

Figure 11. The diagram for each factor influencing the temperature of winding: (**a**) fin height; (**b**) fin width; (**c**) the ratio of slot width to fin width.

The various factors affecting the winding temperature caused by the longitudinal fins are shown in Figure 12. The impact of $H_{\text{f-lf}}$, $W_{\text{f-lf}}$, and $R_{\text{f-lf}}$ on winding temperature is reduced in sequence. As the $H_{\text{f-lf}}$ and $R_{\text{f-lf}}$ increase, the temperature of the motor winding gradually decreases. Conversely, as the $W_{\text{f-cf}}$ increases, the temperature rise in the motor winding also increases gradually. It can be seen that among these three factors, increasing $H_{\text{f-lf}}$ has the most significant effect.

Figure 12. The diagram for each factor influencing the temperature of winding: (**a**) fin height; (**b**) fin width; (**c**) the ratio of slot width to fin width.

The circular fins with small fin width, high fin height, and small slot width have better performance; the longitudinal fins with high fin height, small fin width, and a certain amount of slot width have better performance. Overall, a comparison between the two types of fins shows that the heat transfer performance of longitudinal fins is better than that of circular fins. The optimal combination within the above range was calculated. The maximum winding temperature of the circular fins at $H_{\text{f-f}}$ of 5 mm, $W_{\text{th-cf}}$ of 1 mm, and $R_{\text{hw-cf}}$ of 1 is 349.85 K. The maximum winding temperature of the longitudinal fins at $H_{\text{f-cf}}$ of 5 mm, $W_{\text{th-cf}}$ of 1 mm, and $R_{\text{hw-cf}}$ of 4 or 5 is 333.15 K.

5. The Ratio of Thrust-to-Temperature Rise

From the analysis provided earlier, it was recognized that enhancing the heat dissipation of the ducted fan motor can be effectively achieved by improving the motor casing. However, it is important to note that the presence of fins in the casing can result in a reduction in the thrust produced by the ducted fan motor. Therefore, striking a balance between improving heat dissipation and preserving thrust output is crucial. In order to

assess the thermal design, this study places particular emphasis on the ratio of thrust-to-temperature rise as a key metric for evaluating the effectiveness of the design. The following is a calculation of the thrust and temperature rise in the ducted fan motor at 10,000 rpm.

The method described in Section 4 is then employed to calculate the motor temperature rise based on this condition. Additionally, the tension of the culvert can be directly assessed by applying the results obtained from Section 3.

The given current has an effective value of 34Arms, and the motor speed is 10,000 rpm. The iron loss of the motor is 1074 W, and the copper loss is 452 W (data sourced from experimental values). The calculation process considered the issue of increasing copper losses with the rise in temperature. The calculation results of motor temperature are shown in Figure 13.
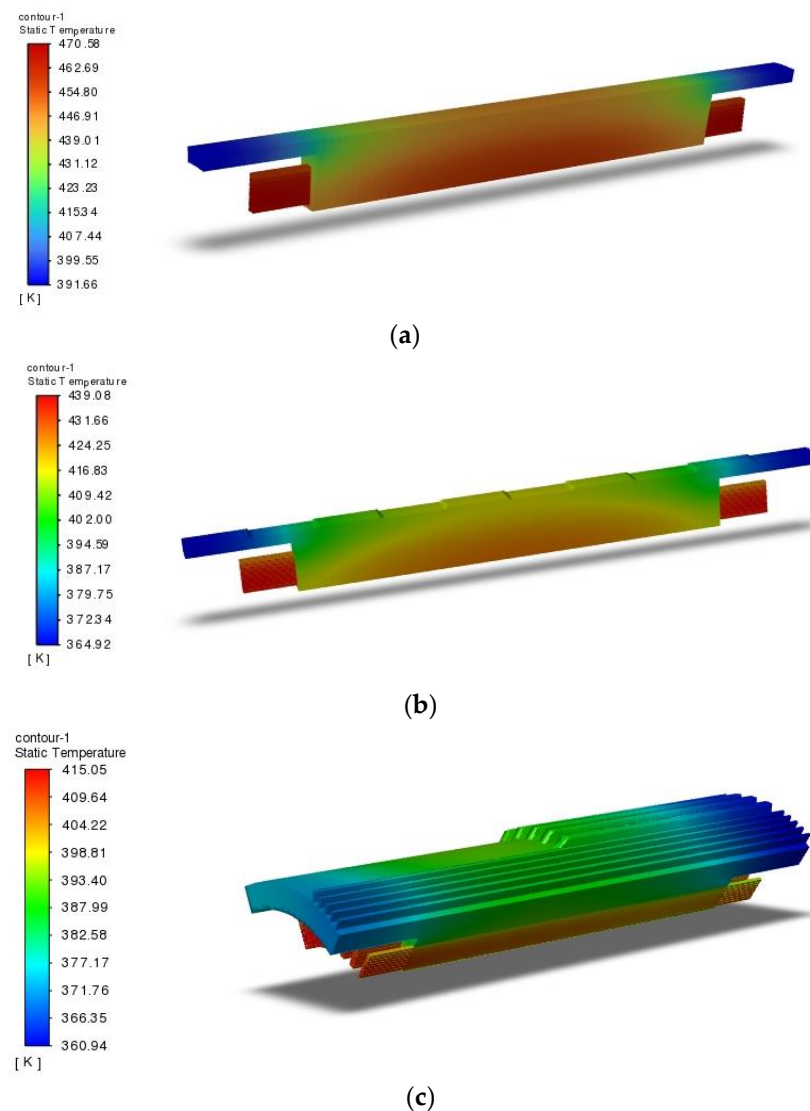
(**a**)

(**b**)

(**c**)

Figure 13. The simulation results of motors: (**a**) the temperature of model 1; (**b**) the temperature of model 2; (**c**) the temperature of model 3.

The ratios of thrust-to-temperature rise in the ducted fan are shown in Figure 14. Model 3 with longitudinal fins has a higher thrust-to-temperature rise ratio, allowing for a higher power output within the same motor winding temperature limit in practical use, thereby enhancing the overall performance of the fan motor system. Analyzing the optimization and improvement of motor cooling reveals its beneficial impact on enhancing

the overall performance of fan motors. Thus, in the later stages of design, it is advisable to prioritize increasing the thrust-to-temperature rise ratio of the fan motor while meeting aerodynamic performance requirements. This approach can lead to better electrical motor performance and higher output power.
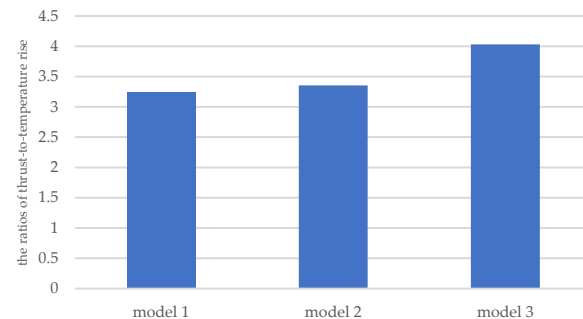

Figure 14. The ratio of thrust-to-temperature rise.

6. Conclusions

This article focuses on the development needs of future flying vehicles and studies the design method of electric drive ducted fan motors.

The coupling model between fan static thrust, motor power, and motor temperature rise was established. When the k_d value is around 0.72, fixing the D_{tip} (outer diameter of propeller hub) to 390 mm is recommended. The optimal k_{out} value, at which both power output and temperature rise criteria are met, is approximately 0.26. Therefore, we optimized a duct fan motor with a D_{tip} of 390 mm, $D_{m,out}$ (outer diameter of motor) of 100 mm, and k_d of 0.7. After confirming the external dimensions of the motor, three cooling schemes of the motor casing were designed. The casing forms are as follows: model 1 with smooth surface, model 2 with circular fins, and model 3 with longitudinal fins.

The static thrust and heat transfer performance were calculated. Adding fins to the casing will decrease the thrust of the ducted fan compared to a smooth casing surface. Longitudinal fins have a greater effect on thrust than circular fins. The thrust of the motor with longitudinal fins decreased by 16.3% compared to that of the motor with a smooth surface. The thrust of the motor with circular fins decreased by 7.2% compared to that of the motor with a smooth surface.

Although the presence of the fins reduces the thrust of the ducted fan, it enhances the motor's cooling performance. Compared to the rise in winding temperature with a smooth surface, with circular fins, it decreases by 18.5%, and with longitudinal fins, it decreases by 30.6%. It is evident that optimizing the heat dissipation on the outer surface of the motor is significantly effective in increasing the power density of the motor.

The optimization work was carried out on the geometric dimensions of two types of fins for model 2 and model 3. Overall, a comparison between the two types of fins shows that the heat transfer performance of longitudinal fins is better than that of circular fins. The maximum winding temperature of the circular fins at H_{f-f} of 5 mm, W_{th-cf} of 1 mm, and R_{hw-cf} of 1 is 349.85 K. The maximum winding temperature of the longitudinal fins at H_{f-cf} of 5 mm, W_{th-cf} of 1 mm, and R_{hw-cf} of 4 or 5 is 333.15 K.

This study proposes the ratio of thrust-to-temperature rise as an indicator for future optimization design of ducted fan motors. Model 3 with longitudinal fins has a higher thrust-to-temperature rise ratio, allowing for a higher power output within the same motor winding temperature limit in practical use, thereby enhancing the overall performance of the fan motor system.

It is advisable to prioritize increasing the thrust-to-temperature rise ratio of the fan motor while meeting aerodynamic performance requirements. This approach can lead to better electrical motor performance and higher output power.

Institutional Review Board Statement: Not applicable.

Informed Consent Statement: Not applicable.

Data Availability Statement: The original contributions presented in the study are included in the article, further inquiries can be directed to the corresponding author.

Conflicts of Interest: The authors declare no conflicts of interest.

References

1. Qian, Y.P.; Luo, Y.W.; Hu, H.Y. Improving the performance of ducted fans for VTOL applications: A review. *Sci. China Technol. Sci.* **2022**, *65*, 2521–2541. [CrossRef]
2. Zhang, Y.; Qian, Y.; Zhuge, W. Progress and key technologies of flying cars. *J. Automot. Saf. Energy* **2020**, *11*, 1–15.
3. Zhang, Y.; Peng, J.; Qian, Y. Key technologies and challenges of hydrogen powered aviation. *Aerosp. Power* **2021**, *1*, 20–23.
4. Wang, K.; Zhou, Z.; Ma, Y. Development and trend analysis of vertical takeoff and landing fixed wing UAV. *Adv. Aeronaut. Sci. Eng.* **2022**, *13*, 1–13.
5. Akturk, A.; Camci, C. Experimental and computational assessment of a ducted-fan rotor flow mode. *J. Aircr.* **2012**, *49*, 885–897. [CrossRef]
6. Patrick, C.V.; Mirko, H. Sizing considerations of an electric ducted fan for hybrid energy aircraft. *Transp. Res. Procedia* **2018**, *29*, 410–426.
7. Xiong, J.H.; Chen, X.; Lang, Y. Key technologies analysis of ducted fan electric. *J. Propuls. Technol.* **2023**, *44*, 1–12.
8. Deng, S.; Wang, S.; Zhang, Z. Aerodynamic performance assessment of a ducted fan UAV for VTOL applications. *Aerospace Sci. Technol.* **2020**, *103*, 105895. [CrossRef]
9. Guo, J.; Zhou, Z.; Li, X. An efficient design method for blade of ducted propeller. *Acta Aeronaut. Astronaut. Sin.* **2022**, *43*, 1–11.
10. Hu, R.; Cao, C.; Zhao, G. Investigations of the layout parameter influence on the aerodynamic characteristics of ducted fan. *Flight Dyn.* **2023**, *41*, 7–12.
11. Sun, P.; Zhou, Z. Fast calculation and optimization of ducted propeller based on slipstream model. *J. Aerosp. Power* **2023**, 1–11. [CrossRef]
12. Li, X.; Guo, Z.; Chen, Q. Numerical simulation of ducted rotor's aerodynamic characteristics. *J. Natl. Univ. Def. Technol.* **2015**, *37*, 31–35.
13. Zheng, Z.; Zhou, Z. Analysis on the estimation model of lift fan when designing Vtol. *Flight Dyn.* **2010**, *28*, 21–23.
14. Li, X.; Guo, Z.; Liu, Z. Influence of ducted fan profile parameters on aerodynamic characteristics. *J. Natl. Univ. Def. Technol.* **2016**, *38*, 28–33.
15. Raj, J.A.P.S.; Asirvatham, L.G.; Angeline, A.A. Thermal management strategies and power ratings of electric vehicle motors. *Renew. Sustain. Energy Rev.* **2024**, *189*, 113874.
16. Ting, Z.; Zhang, Y.; Qiang, L. Overview of hybrid cooling system for high power density motor. *Electr. Eng.* **2022**, *23*, 1–16.
17. Huang, W.; Zhang, Z.; Huang, W. Optimal design of high speed electric ducted fan for private evtol considering specific power and temperature distribution. In Proceedings of the 2021 24th International Conference on Electrical Machines and Systems (ICEMS), Gyeongju, Republic of Korea, 31 October–3 November 2021.
18. Hu, X.; Qian, Y.; Dong, C. Thermal Benefits of a Cooling Guide Vane for an Electrical Machine in an Electric Ducted Fan. *Aerospace* **2022**, *9*, 583. [CrossRef]
19. Huang, W.; Zhang, Z.; Da, X. Research on thermal characteristics of dual drive motors for high speed counter rotating ducted fan. *Acta Aeronaut. Astronaut. Sin.* **2024**, *25*, 1–14.
20. Yu, L.; Xiong, J.; Chen, X. Design and test of forced air cooling structure for ducted fan motor. *Micro Electr. Mot.* **2024**, *52*, 7–13.
21. Chen, Y.; Chen, P.; Wang, Z. Magnetic thermal coupling simulation analysis of kx-zm01 ducted fan BLDC motor. *Mech. Electr. Eng. Technol.* **2022**, *51*, 165–169.
22. Jin, Y.; Qian, Y.; Zhang, Y. Modeling of ducted-fan and motor in an electric aircraft and a preliminary integrated design. *SAE Int. J. Aerosp* **2018**, *11*, 1–12. [CrossRef]
23. Ma, T.; Zhang, Y.; Wang, Z. Design Sensitivity Analysis and Optimization of Flexible Coupling Based on Orthogonal Test. *J. Propuls. Technol.* **2022**, *2*, 231–239.

24. Li, Y.; Shen, C.; Zhu, J. *Experiment Design and Data Processing*; Chemical Industry Press: Beijing, China, 2008; pp. 124–158.
25. Li, Y.; Fan, T.; Wen, X. Numerical research on hydraulic and thermal performance of the motor water jackets based on the orthogonal experiment. In Proceedings of the International Conference on Electrical Machines & Systems, Busan, Republic of Korea, 26–29 October 2013.